RSC Advances

PAPER

View Article Online
View Journal | View Issue

Cite this: *RSC Adv.*, 2022, **12**, 31923

Enhanced pseudocapacitive energy storage and thermal stability of Sn^{2+} ion-intercalated molybdenum titanium carbide (Mo_2TiC_2) MXene†

Irfan Ali, Zulqarnain Haider and Syed Rizwan *

Received 3rd September 2022
Accepted 24th October 2022

DOI: 10.1039/d2ra05552j

rsc.li/rsc-advances

Electrochemical energy-storage (EES) devices are a major part of energy-storage systems for industrial and domestic applications. Herein, a two-dimensional (2D) transition metal carbide MXene, namely Mo_2TiC_2, was intercalated with Sn ions to study the structural, morphological, optical, and electrochemical energy-storage effects. The Sn^{2+}-intercalated modified layered structure, prepared *via* a facile liquid-phase pre-intercalated cetyltrimethylammonium bromide (CTAB) method, showed a higher surface area of 30 $m^2\ g^{-1}$, low band gap of 1.3 eV, and large interlayer spacing of 1.47 nm, as compared to the pristine Mo_2TiC_2. The Sn@Mo_2TiC_2 electrode showed a high specific capacitance of 670 F g^{-1}, representing a large diffusion control value compared to pure Mo_2TiC_2 (212 F g^{-1}) at a scan rate of 2 mV s^{-1}. The modified electrode also presented long-term cyclic performance, high-capacity retention and coulombic efficiency measured over 10 000 cycles. The Sn@Mo_2TiC_2 electrode showed much improved electrocatalytic efficiency, which may open up ways to employ double-transition 2D MXenes in energy-storage devices.

Introduction

The rising demands for energy across the globe, and the reducing resources of fossil fuels and their harmful impact on the environment have urged engineers, scientists, and researchers to investigate new renewable sources of energy generation. Solar and wind power systems are two major sources of renewable energy, which are efficient, clean, and environmentally friendly with great potential to fulfill future energy requirements. A key hurdle in their way, however, is how to manufacture some efficient energy-storage devices at the domestic as well as an industrial level.[1] For this purpose, lithium-ion batteries are playing a key role at a commercial scale, but like fossil fuels, the sources of lithium metal are limited, and they also suffer from low energy density and high cost.[2–6] So, keeping in mind the present energy usage scenario, scientists are engaged in pushing the research in two major directions: to improve the already built energy-storage systems and develop new efficient high energy-density systems.[7]

Electrochemical energy-storage (EES) devices are attracting the attention of researchers due to their high energy-storage capacity, cyclic stability, and fast kinetics, which have made it possible to use these systems in all kinds of electronic gadgets, hybrid electric vehicles, and grid-storage applications.[8–10] Two-dimensional (2D) materials are the most suitable candidates for EES devices due to their improved physical and chemical properties. A wide range of 2D materials has been reported, including graphene, metal dichalcogenides, oxides, sulfides, and nitrides.[11–18]

One of the most recent advancements in the field of 2D materials is related to transition metal carbides or nitrides, also known as MXenes, which were reported for the first time in 2011.[19] These MXenes are directly synthesized from the MAX phase by the selective etching of the A atomic layer in HF etching solution for the optimum time, wherein the general formula describes the composition of MAX, which is written as $M_{n+1}AX_n$, where M is an early transition metal, A belongs to group IIIA or IVA elements, and X is a carbon or nitrogen element, and $n = 1$, 2, or 3.[20] The exfoliated MXenes have the general formula $M_{n+1}\ X_n\ T_x$, where T_x defines the surface terminations (OH, F, and O) associated with MXenes and x denotes the number of termination groups. MXenes have lot of applications in the field of energy storage,[21–39] biosensing,[40,41] electromagnetic interference shielding,[42,43] water purification,[44] ion sieving,[45] and anti-bacterial activities.[46,47] MXenes show pseudocapacitive behavior when used in supercapacitor applications.

Physics Characterization and Simulations Lab (PCSL), Department of Physics, School of Natural Sciences (SNS), National University of Sciences and Technology (NUST), Islamabad 44000, Pakistan. E-mail: syedrizwan@sns.nust.edu.pk; syedrizwanh83@gmail.com

† Electronic supplementary information (ESI) available: Some important formulas for calculation of the electrochemical parameters are provided in the supplementary information. See DOI: https://doi.org/10.1039/d2ra05552j

In the presence of termination groups (F and OH) on the surface of MXenes, their surface behaves as a negatively charged MXene.[48] Therefore, due to the negatively charged surface of MXenes, some metal cations are easily intercalated between the MXene layers due to electrostatic interactions.[49] This pillared process helps to rectify the restacking issue among the MXene layers, which restricts the cyclic stability of MXenes. Pillared intercalated clays (PILCs) are the most common and important examples of the pillaring effects in nanostructures due to their applications in separation and catalysis.[50,51] PILCs show a large interlayer space due to the stable pillaring effect among the layers of clays.[52]

Luo *et al.* prepared hybrid electrodes by using Ti_3C_2 MXenes for high-performance lithium-ion capacitors and a sodium metal anode, whereby they obtained better results compared to pure Ti_3C_2 MXene.[53,54] Maughan *et al.* also synthesized the silica-pillared Mo_2TiC_2 MXene, which shows better performance for Li- and Na-ion batteries, and also synthesized *in situ* pillared MXene for zinc-ion hybrid capacitor applications.[55,56]

Inspired by the above-mentioned idea, we prepared the Sn-intercalated nanostructure ($Sn@Mo_2TiC_2$) with improved electronic conductivity, large surface area, and good ion-diffusion properties. The CTAB surfactant was used for pre-intercalation because Mo_2TiC_2 does not form a homogeneous solution in deionized water due to its high surface resistance, while the pre-intercalated long-tailed CTA^+ cation provides an easy way to intercalate Sn^{2+} among the layers of Mo_2TiC_2 MXenes and in the presence of surfactant, and the absorbed Sn^{2+} spread uniformly among the layers of Mo_2TiC_2 nanocomplex, whereas without the surfactant it was difficult to intercalate Sn^{2+} on MXene nanosheets.[57] The Sn^{2+}-intercalated Mo_2TiC_2 offers more surface area due to the large interlayer space that helps to store a larger number of charges among the 2D gallery heights of the MXenes. Meanwhile, in the presence of Sn^{2+}-intercalated Mo_2TiC_2 hybrid ($Sn@Mo_2TiC_2$), the surface and layered structure of the MXene became more conductive. Another important advantage of Sn^{2+} pillaring among the layers of MXenes was the volume expansion, which further enhances the electrochemical stability by rectifying the restacking issue among the sheets and provides more active sites for the storage of charges even at high scan rates.[53] The prepared electrode for supercapacitor applications has a high cyclic stability and specific capacitance value as compared to pure Mo_2TiC_2 MXene.

Experimentation

The whole process used for the synthesis of the $Sn@Mo_2TiC_2$ nanostructure was like that reported by Luo *et al.*[53,54] with some modifications, as described in Fig. 1.

Synthesis of Mo_2TiC_2 MXene

MAX phase Mo_2TiAlC_2 (200 mesh) powder was purchased from Yiyi Technology (Jilin Province Yiyi Technology Co., Ltd, Jilin, China) and directly used for the synthesis of Mo_2TiC_2 MXene through a conventional method. For this purpose, 1 g of MAX powder was added into 10 ml 50% concentrated solution of hydrofluoric acid (HF) and the mixture was continuously stirred in a Teflon beaker at 250 rpm for 72 h at 55 °C. The Mo_2TiC_2 obtained through this process was centrifuged and washed with deionized water several times at 3500 rpm until the pH reached 6, and finally, the powder was collected by vacuum filtration and dried under vacuum at 60 °C for 24 h.

Synthesis of the $Sn@Mo_2TiC_2$ hybrid

For the preparation of the $Sn@Mo_2TiC_2$ nanostructure, 200 mg Mo_2TiC_2 was stirred in 40 ml CTAB (0.150 wt%) solution for 24 h at room temperature. Then $SnCl_2{-}2H_2O$ (Sinopharm Chemical Reagent Co. Ltd.) was added (13.536 mg) to prepare 1.5 mM solution and again stirred for 12 h under the same conditions.

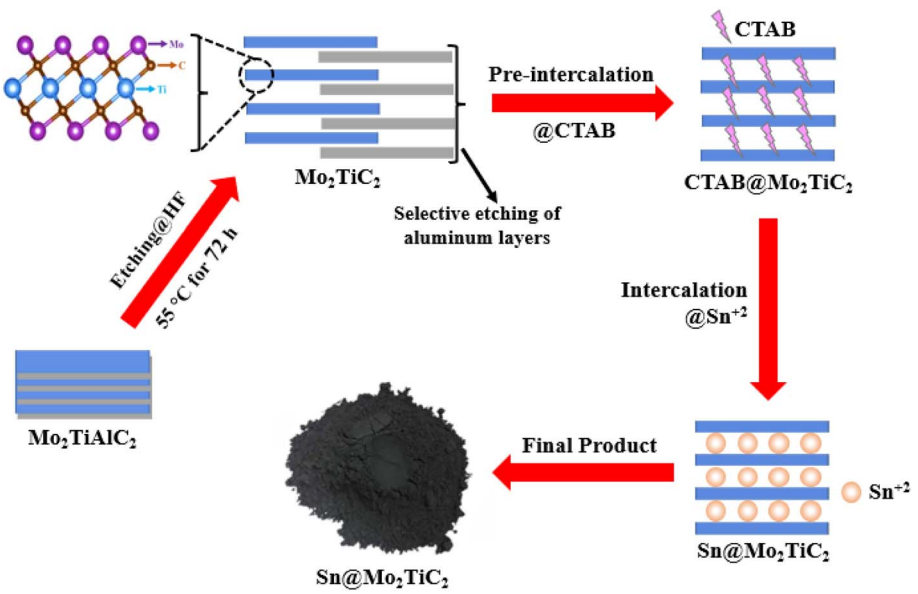

Fig. 1 Schematic diagram for the synthesis of the $Sn@Mo_2TiC_2$ nanohybrid.

Finally, the product collected was rinsed with water and dried under a vacuum at 60 °C for another 24 h.

Material characterization

To study the structural properties of the nanohybrid, an X-ray diffractometry system (XRD, Bruker, D8 Advance) with a monochromatic Cu-Kα source and wavelength of 1.54 Å was used. The thermal stability of the nanohybrid was determined by thermogravimetric analysis (TGA, SDT650) and an ultraviolet–visible (UV–vis, Lambda 365 PerkinElmer) absorption test was performed to estimate the band gap of the nanostructure. To study the surface area and average pore volume of the hybrid material, gas adsorption–desorption analysis based on the Brunauer–Emmett–Teller (BET, Quantachrome NovaWin) method was performed. The morphological properties of the materials were analyzed by scanning electron microscopy (SEM; Hitachi s-4800 FEG), while energy dispersive X-ray spectroscopy (EDX) was used to measure the elemental composition of the material. Fourier transform infrared (FTIR, Bruker Alpha) spectrometry was used to study the chemical structure of the samples. Raman spectrometry (Thermo Renishaw, He–Ne laser, $\lambda = 532$ nm) was employed to study the chemical bond structure of the nanohybrid.

Electrochemical measurements

Electrochemical measurements were determined by using a potentiostat electrochemical workstation (Gamry 1010B) three-electrode system, in the presence of 1 M KOH electrolyte solution. The counter and reference electrodes consisted of platinum wire and Ag/AgCl, respectively. The working electrode was prepared by the following steps. To study the electrochemical properties of our hybrid electrode, we used Ni foam as a current collector. For that purpose, we made a slurry of $Sn@Mo_2TiC_2$ nanohybrid by using 75% active material, 15% carbon black, 10% polyvinylidene fluoride (PVDF), and *N*-methylpyrrolidone (NMP) used as a solvent. The as-prepared slurry was coated on the Ni foam of a 1 cm × 1 cm current collector, which was prewashed sequentially with hydrochloric acid, ethanol, and deionized water by using a sonicator. Finally, the Ni foam electrode was dried in a vacuum oven overnight and pressed under 5 Mpa pressure for 10 s. Cyclic voltammetry (CV) tests were performed at different scan rates to study the electrochemical behaviors of the samples and the gravimetric capacitance. The long-term cyclic performances of the electrodes were studied by galvanostatic charge–discharge (GCD) tests at a current density of 10 A g^{-1} for 10 000 cycles. To study the charge-transfer resistance and diffusion coefficient of the samples, electrochemical impedance spectroscopy (EIS) measurements were performed in the frequency range of 20 kHz to 10 mHz at open circuit voltage (OCV), with a sinusoidal signal of 10 mV.

Results and discussion

The X-ray diffraction (XRD) patterns of the MAX phase, MXene, and Sn-intercalated MXene are presented in Fig. 2a. The results obtained from the XRD data were in good agreement with the earlier reports, which evidenced the successful synthesis of Mo_2TiC_2 MXene from the Mo_2TiAlC_2 MAX phase.[58,59] The peak values of the planes (002), (004), and (006) in Mo_2TiC_2 were shifted toward lower diffraction angles of 6.8°, 13.6°, and 18.9° compared to the parent MAX phase (9.4°, 19°, and 28.6°), which signified an increase in the *c*-lattice parameter (*c*-LP) due to the surface functional groups and adsorption of water molecules between the Mo_2TiC_2 layers.[60]

The main peak of the 002 plane was further shifted to a lower angle from 6.8° to 6.0° in the case of Mo_2TiC_2 MXene to $Sn@Mo_2TiC_2$, which presented that Sn^{2+} intercalation enhanced the *c*-LP from 25.8 to 29.3 Å and d-spacing from 1.29 nm to 1.47 nm. The increase in the *c*-LP and *d* value of the 002 plane for $Sn@Mo_2TiC_2$ confirmed the successful Sn^{2+} intercalation among the layers of Mo_2TiC_2 MXene nanosheets. The value of the peak intensity was also observed to decrease for the (002) plane in the case of the $Sn@Mo_2TiC_2$ hybrid compared to pure Mo_2TiC_2 and the 006 peaks also vanished, which also suggested the amorphous nanocomplex formed on Mo_2TiC_2. The interaction between Mo_2TiC_2 was further confirmed from the peak split in the FTIR spectra of pure Mo_2TiC_2 and $Sn@Mo_2TiC_2$, as shown in Fig. 4a.

Thermogravimetric (TGA) analysis was performed to investigate the thermal properties of the materials to estimate the thermal conductivity, thermal stability, and thermal expansion. TGA measurements for Mo_2TiAlC_2, Mo_2TiC_2, and $Sn@Mo_2TiC_2$ were carried out in the range from room temperature (RT) to 800 °C in the presence of N_2 gas, as shown in Fig. 2b. The MAX phase was thermally stable throughout the temperature range, except for a little weight gain in the range of 600 °C to 800 °C, which may have been due to the selective oxidation of Al while heating in N_2 in the presence of a minor oxygen content.[61] The Mo_2TiC_2 MXene was also found to be thermally stable throughout the temperature range (RT to 800 °C), except for a slight gradual decrease in weight of up to 1%, which was due to the unstable surface functional groups, like –F, –O, and –OH. $Sn@Mo_2TiC_2$ was also heated in an N_2 environment in the same temperature range and an initial weight loss of about 2% was observed between 200 °C to 500 °C, which may have been due to the removal of the CTAB surfactant. A further rapid weight loss of up to 5% was also observed between the temperature range of 500 °C to 590 °C, after which it remained stable.

This was the temperature range where the intercalated MXene showed the worst resistance to thermal degradation. However, most reported MXene nanostructures are stable only up to 350 °C and so our material is thermally more stable.[62,63] The results of the TGA were strongly consistent with the XRD data, which confirmed the successful intercalation of the amorphous nanocomplex on Mo_2TiC_2 MXene.

The differential scanning calorimetry (DSC) curves for Mo_2TiAlC_2, Mo_2TiC_2, and $Sn@Mo_2TiC_2$ are also shown in Fig. 2c. It was observed that all the samples showed their initial peak around 110 °C, which suggests that the change in mass rate happened in all the samples at that point due to the loss of the minor moisture content among the layered structures and a relative endothermic heat flow reaction occurred. A similar

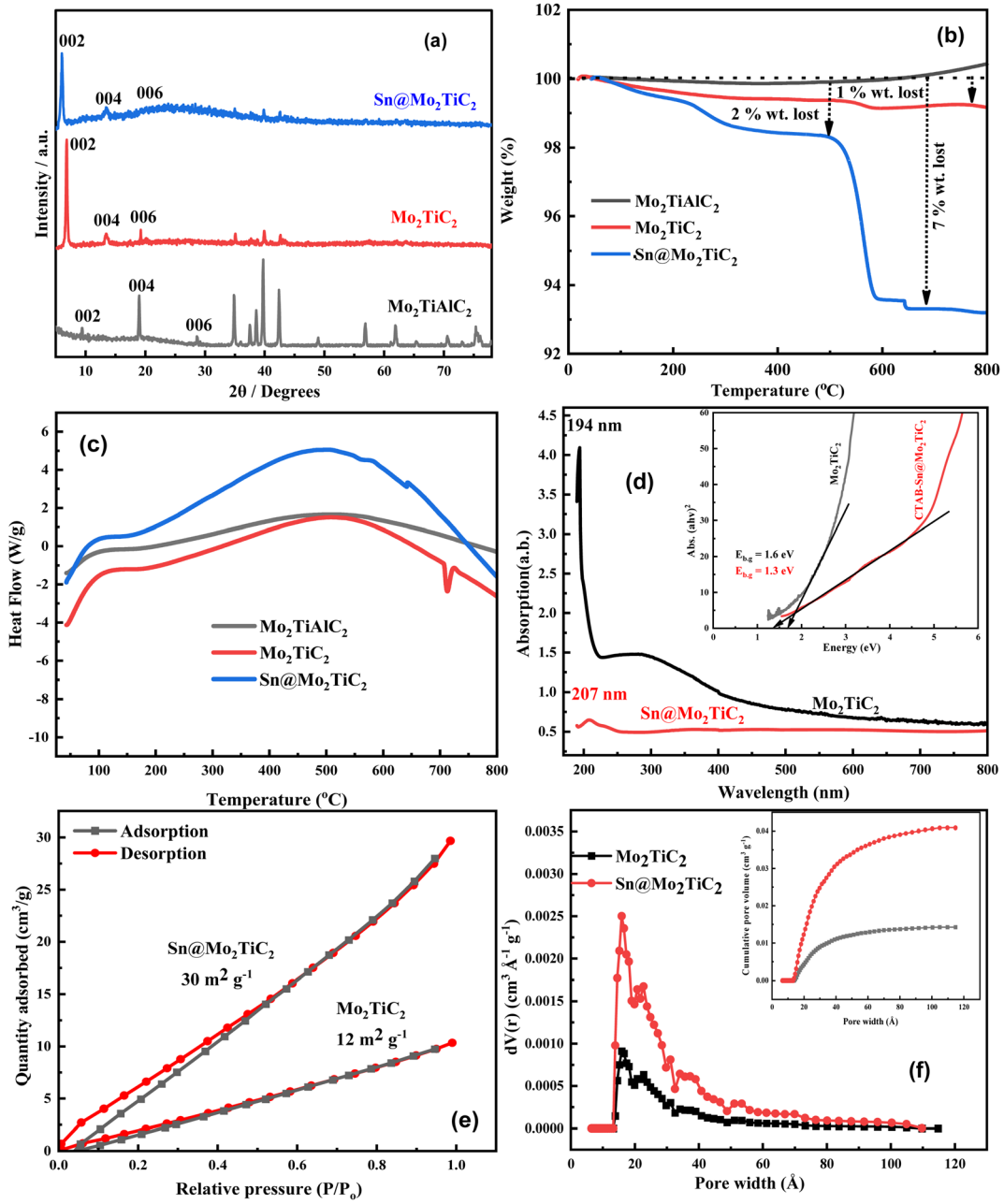

Fig. 2 (a) XRD plots for Mo_2TiAlC_2, Mo_2TiC_2, and the $Sn@Mo_2TiC_2$ nanohybrid, (b) TGA plots for Mo_2TiAlC_2, Mo_2TiC_2, and $Sn@Mo_2TiC_2$, (c) DSC curves for Mo_2TiAlC_2, Mo_2TiC_2, and $Sn@Mo_2TiC_2$, (d) UV-visible absorption spectra and inset Tauc plots for both Mo_2TiC_2 and $Sn@Mo_2TiC_2$, (e) N_2 adsorption–desorption plots at 77 k for Mo_2TiC_2 and the $Sn@Mo_2TiC_2$ nanohybrid, (f) pore-size distribution, (inset cumulative pore volume graph past) *vs.* the pore width calculated through the NL DFT method for both the samples Mo_2TiC_2 and $Sn@Mo_2TiC_2$.

kind of large peak was observed in the DSC data around 500 °C in all the samples, but it was more prominent in the case of Mo_2TiC_2 and $Sn@Mo_2TiC_2$ because the rate of mass loss was more significant in the Mo_2TiC_2 and $Sn@Mo_2TiC_2$ structures as compared to the very small mass gain rate in Mo_2TiAlC_2, which further indicated that a large endothermic heat flow occurred among the material structures due to the change in the mass loss rate. As we already discussed in the TGA results, the mass loss was due to the unstable surface termination groups and low thermal degradation resistance, respectively, at high temperature.[59]

UV-vis spectroscopic analysis was performed to study the optical properties of our structures. The results are shown in Fig. 2d, which exhibit that the peak values for the absorption of Mo_2TiC_2 and $Sn@Mo_2TiC_2$ were obtained at 194 and 207 nm, respectively. The shift in peak positions identified that the band gap was reduced after adding Sn^{2+} in MXene, which might be due to some new states' formation between the valence and conduction bands. The inset Tauc plot curve was also plotted to

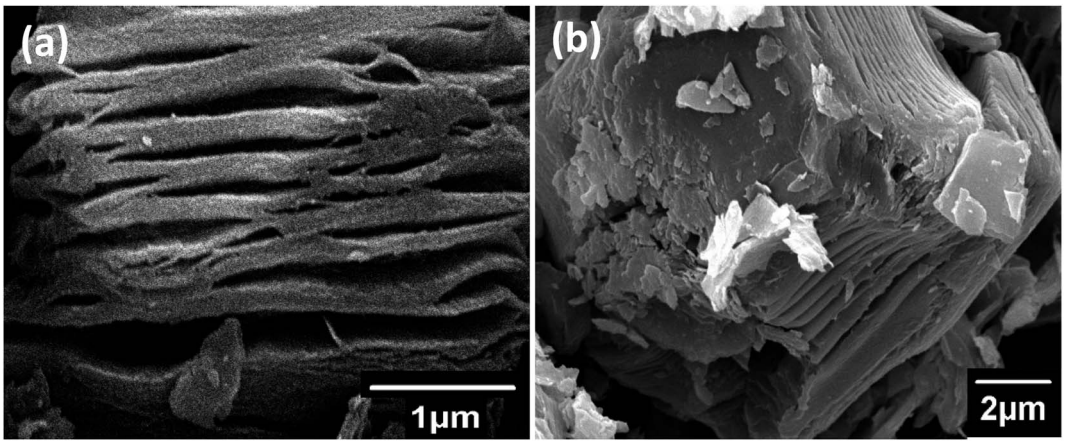

Fig. 3 Scanning electron microscopy (SEM) images of both the samples (a) Mo_2TiC_2 MXene image taken at 1 μm, (b) Sn@Mo_2TiC_2 hybrid image taken at 2 μm.

calculate the value of the band gaps of Mo_2TiC_2 and Sn@Mo_2TiC_2, which varied from 1.6 eV (for pristine MXene) to 1.3 eV (for Sn-intercalated MXene). This result is an indication of the successful intercalation of Sn^{2+}.[64]

To study the effect of Sn^{2+} on the surface area of the MXene, BET analysis was performed in the presence of N_2 isotherm at 77 K. Fig. 2e shows the results of the adsorption–desorption data for both the samples Mo_2TiC_2 and Sn@Mo_2TiC_2. Fig. 2e shows that the surface area for the nanohybrid (Sn@Mo_2TiC_2) increased up to 30 $m^2\ g^{-1}$ compared to 12 $m^2\ g^{-1}$ for pure Mo_2TiC_2 MXene, which indicated that the hybrid material had a more porous nature compared to pure MXene. Fig. 2f shows the pore-width distribution, which was calculated through the non-local density functional theory (NL DFT) method and inset plot of the cumulative pore volume *vs.* pore width.[65] The results of the inset plot of Fig. 2f show that the pore volume increased from 0.015 to 0.042 $cm^3\ g^{-1}$, which was again consistent with the BET results (whereby the surface area increased from 12 to 30 $m^2\ g^{-1}$). Hence the increase in porosity of the Sn@Mo_2TiC_2 was increased due to the interaction of Sn^{2+} with the Mo_2TiC_2 nanosheets. These results were also consistent with the XRD data of Mo_2TiC_2 and Sn@Mo_2TiC_2, where a shift in diffraction angle toward the lower side was observed in the main peak of the 002 plane for both the samples, and as a result the *c*-LP values were increased from 2.58 to 2.93 nm, respectively (Mo_2TiC_2 to Sn@Mo_2TiC_2). So, the increase in *c*-LP also became the cause of the increase in *d* value from 1.29 to 1.47 nm for Mo_2TiC_2 to Sn@Mo_2TiC_2. Finally, we can say that the increase in the surface area of our hybrid material was basically due to the interaction of Mo_2TiC_2 with Sn^{2+}.

The surface morphology of the Mo_2TiC_2 MXene and Sn@Mo_2TiC_2 was studied by scanning electron microscopy (SEM), as shown in Fig. 3 a and b. Both the SEM micrographs of MXene and the hybrid material Sn@Mo_2TiC_2 (1 and 2 μm) showed a layered nature, respectively. Fig. 3b shows presence of Sn^{2+} in the prepared sample. In addition, Sn^{2+} was noted in the spectra, confirming its presence in the hybrid (ESI Fig. S2†).

Moreover, the SEM image for the hybrid material showed that the Sn^{2+} intercalation did not destroy the layered structure of MXene in Sn@Mo_2TiC_2, which was also confirmed by the

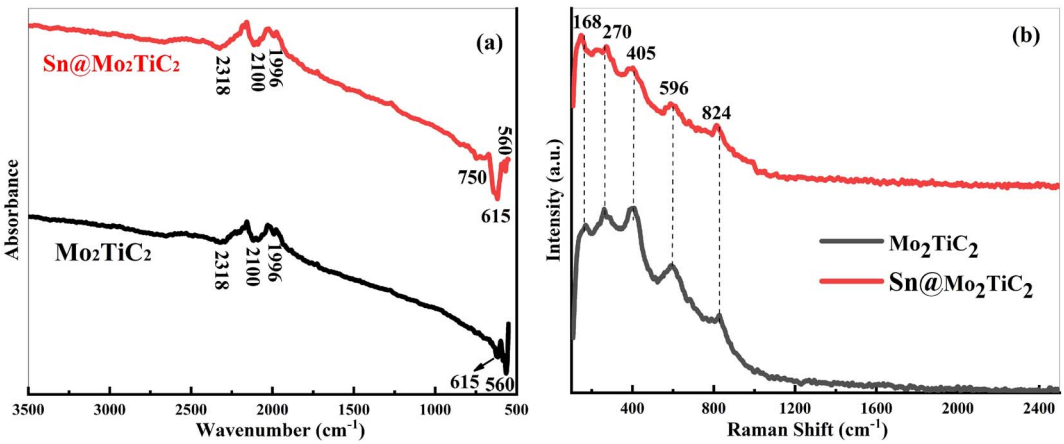

Fig. 4 (a) FTIR spectra of Mo_2TiC_2 and the Sn@Mo_2TiC_2 nanohybrid, (b) Raman spectra of Mo_2TiC_2 and the Sn@Mo_2TiC_2 nanohybrid.

XRD data (Fig. 2a). SEM energy dispersive X-ray spectroscopy (EDX) was also performed to confirm the Sn^{2+} content in the $Sn@Mo_2TiC_2$ hybrid in (wt%) percentage along with the EDX spectra. The EDX spectra and elemental composition of both the samples along with their SEM images are displayed in Fig. S1 and S2 in the (ESI) data,† where the small peaks corresponding to aluminum showed the presence of a small fraction of the unreacted MAX phase in the MXene sample. The unfitted peak to the left of the Mo peak is a continuum (background). The EDX results also confirmed the presence of F and O surface termination groups.

FTIR spectroscopy was used to confirm the successful Sn^{2+}-exchange absorption phenomenon on the Mo_2TiC_2 MXene. Fig. 4a shows the FTIR spectra of Mo_2TiC_2 before and after treating it with $SnCl_2{\cdot}2H_2O$ solutions. The peaks observed at 2318, 2100, and 1996 cm^{-1} belonged to the stretching vibration of the bonds C=O, C≡C, and C=C, respectively, as shown in Fig. 4a.[66] The main two peaks at 615 and 560 cm^{-1} were due to the deformation molecular vibrations of Ti–O and Mo–O in the case of the Mo_2TiC_2 sample. However, a new peak appeared at 750 cm^{-1} in the case of $Sn@Mo_2TiC_2$, which was due to Sn–O bond vibrations.[37] Basically, the split in the peak around 750 was due to the successful intercalation of the amorphous nanocomplex among the layers of MXene.

Fig. 4b shows the Raman spectra of Mo_2TiC_2 and the $Sn@Mo_2TiC_2$ MXene nanohybrid. The peaks that appeared at 168, 270, 405, 596, and 824 cm^{-1} closely matched with the previously published data and no significant difference appeared in the peak positions observed after interaction with Sn^{2+}.[55] The peak that appeared around 168 cm^{-1} was due to the E_g mode of vibrations of both Mo and Ti atoms in the presence of the –O terminated Mo_2TiC_2 MXene. The peak at around 270 cm^{-1} appeared due to the E_g vibration due to oxygen. The other three peaks at 405, 596, and 824 cm^{-1} suggested the vibrations of carbon atoms present in the MXene structure. In literature, Kim *et al.* assigned the peak that appears at 405 cm^{-1} to –O vibrations, but Chen *et al.* assigned it to –C vibrations.[67,68] Fig. 4a also shows that no new peak appeared after the intercalation of Sn^{2+}, which is again evidence that the amorphous nanocomplex formed on Mo_2TiC_2 due to interaction with Sn^{2+}, so the results of the Raman spectra were also consistent with the XRD results.

Cyclic voltammetry

The electrochemical performance was studied by cyclic voltammetry. Fig. 5a and b show the CV plots for Mo_2TiC_2 MXene and $Sn@Mo_2TiC_2$ at different scan rates of 2, 5, 10, 20, 50, 100, 150, and 200 mV s^{-1} under a specific potential window. Two peaks were observed at all scan rates, namely due to the electrochemical insertion of K^+ ions (cathodic peak) and the extraction of K^+ ions called the anodic peak, indicating the successful electrochemical process. The oxidation and reduction reactions showed some specific values of voltages for all the scan rates. The average oxidation and reduction potential for Mo_2TiC_2 and $Sn@Mo_2TiC_2$ were 0.41, 0.42 V and 0.30, 0.25 V, respectively, suggesting the presence of a strong faradaic phenomenon in both electrodes.[69] These CV curves indicated that by increasing the scan rate, the value of the current increased, according to the relation in the ESI (SI1†), but the value of the electrochemical capacitance decreased due to the lesser interaction of the electrolyte with the electrode at high scan rates. Moreover, the value of gravimetric capacitance was observed to be higher in $Sn@Mo_2TiC_2$ because Sn^{2+} interaction with MXene provided sufficiently high electroactive sites for easy electrolyte transportation and enhanced the effective surface area for better electrochemical kinetics at all the scan rates compared to the pristine MXene. Hence, the highest value of gravimetric capacitance was observed for both samples at a scan rate of 2 mV s^{-1}, which was 212 F g^{-1} for Mo_2TiC_2 and 670 F g^{-1} for $Sn@Mo_2TiC_2$. These results show that the value of specific capacitance increased for the Sn-intercalated electrode, which may be due to its large charge-storage ability owing to the pillaring effect. The formula used to measure the values of specific capacitance is given in the ESI(SI2†).[70,71]

Fig. 5c shows the plot between $\log I_p$ and $\log \nu$ to measure the b values for Mo_2TiC_2 and $Sn@Mo_2TiC_2$, where I_p represents the peak current, and ν is used for the scan rate (SI3†). Generally, the value of $b = 1$ or 0.5 (where $b = 1$ represents the capacitive process and $b = 0.5$ indicates the diffusion control dominated process), but most of the time, the value of the b parameter lies between 1 and 0.5, which is evident of a combined charge-storage mechanism.

Here we measured the value of b for both the samples Mo_2TiC_2 and $Sn@Mo_2TiC_2$ ($b = 0.727$ and $b = 0.691$), respectively, as shown in Fig. 5c, where the slightly low b value of our as-synthesized hybrid electrode indicated that it was a more diffusion control process as compared to Mo_2TiC_2, which indicated that there were some more active sites available for charge storage in the hybrid material due to its porous nature. Meanwhile, the value of b (0.69) ranged between 1 and 0.5 for the hybrid electrode $Sn@Mo_2TiC_2$, revealing that the electrochemical reaction kinetics were associated with both charge-storage mechanisms for the diffusion control process and capacitive-like effects as well. Fig. 5d shows the plot between the specific capacity (F g^{-1}) and scan rate (mV s^{-1}) for Mo_2TiC_2 and $Sn@Mo_2TiC_2$. The values of the hybrid electrode were found to be higher at all the scan rates in comparison to Mo_2TiC_2 MXene. Here we see that the specific capacities of both electrodes decreased at high scan rates, which was due to the limitations of the reaction kinetics.

To study the combined charge storage mechanism further due to the capacitive process and diffusion control, we used the relation (SI4) in the ESI† where the total peak current I_p is divided into $k_1\nu$ (capacitive process) and $k_2\nu^{0.5}$ (diffusion control process), which represent the contribution of the charge-storage mechanism in both ways. Furthermore, the values of k_1 and k_2 could be determined by plotting a graph between $I_p\,\nu^{-0.5}$ and $\nu^{0.5}$,[72] as given in SI5 in the ESI.† The slope represents the k_1 value and the point of the intercept defines the value of k_2. We measured all these values for both the samples of Mo_2TiC_2 MXene and $Sn@Mo_2TiC_2$. After calculating the percentage contributions of the diffusion and capacitive process values for both Mo_2TiC_2 and $Sn@Mo_2TiC_2$

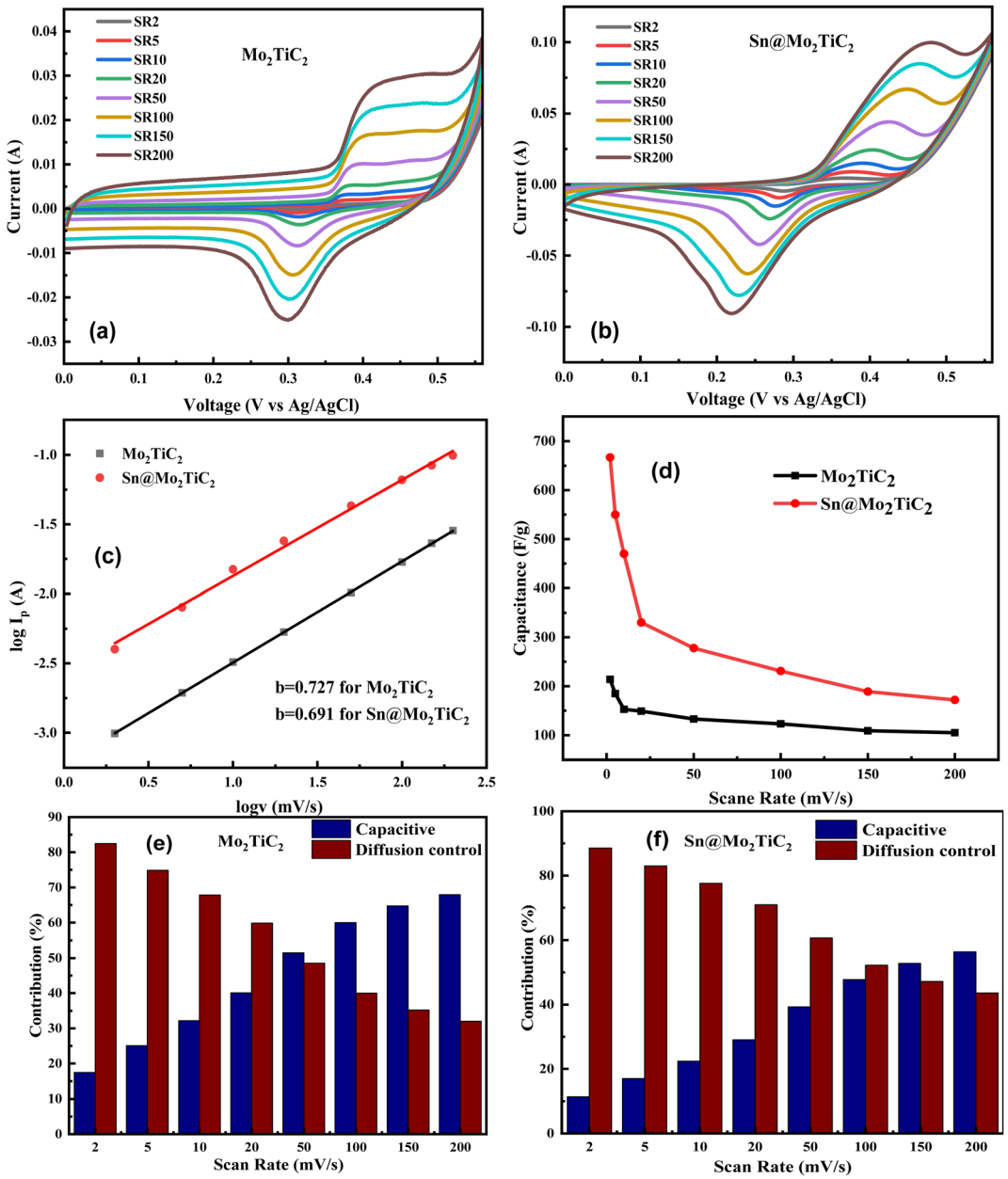

Fig. 5 CV plots using 1 M KOH electrolyte for (a) Mo_2TiC_2 MXene and (b) the Sn@Mo_2TiC_2 nanohybrid at different scan rates. (c) Combine *b* value plots for both Mo_2TiC_2 and the Sn@Mo_2TiC_2 nanohybrid. (d) Scan rate *vs.* capacitance the F g^{-1} plot for both Mo_2TiC_2 and the Sn@Mo_2TiC_2 nanohybrid, (e) plots between the scan rate and percentage contribution of Mo_2TiC_2 for the capacitive and diffusion control processes, (f) plots between the scan rate and percentage contribution of the Sn@Mo_2TiC_2 nanohybrid for the capacitive and diffusion control processes.

at all scan rates (2 to 200 mV s^{-1}), we plotted the results in Fig. 5 e and f.

The percentage contributions of the diffusion and capacitive process of Mo_2TiC_2 MXene and Sn@Mo_2TiC_2 showed that the value of diffusion control was high at low scan rates, which was due to the maximum interaction of the electrolyte ions with the electrodes as compared to at a high scan rate. By comparing the results of the diffusion control and capacitive process contributions for both the samples Mo_2TiC_2 MXene and Sn@Mo_2TiC_2, it could be concluded that the value for diffusion control was improved in the case of the hybrid electrode Sn@Mo_2TiC_2 from 82% to 88% and 32% to 43% at scan rates of 2 to 200 mV s^{-1} compared to Mo_2TiC_2. This evidence indicates that the electrochemical reaction kinetics dominated due to the diffusion control process in our as-synthesized hybrid electrode. The increase in the diffusion process contribution was also observed in the Sn^{2+}-treated Mo_2TiC_2, which was due to the larger surface area, large spacing among the layers of MXene, and high electronic conductivity of the hybrid electrode.

Fig. 6a shows the higher values of the anodic and cathodic peak currents at all scan rates for the Sn@Mo_2TiC_2 electrode as

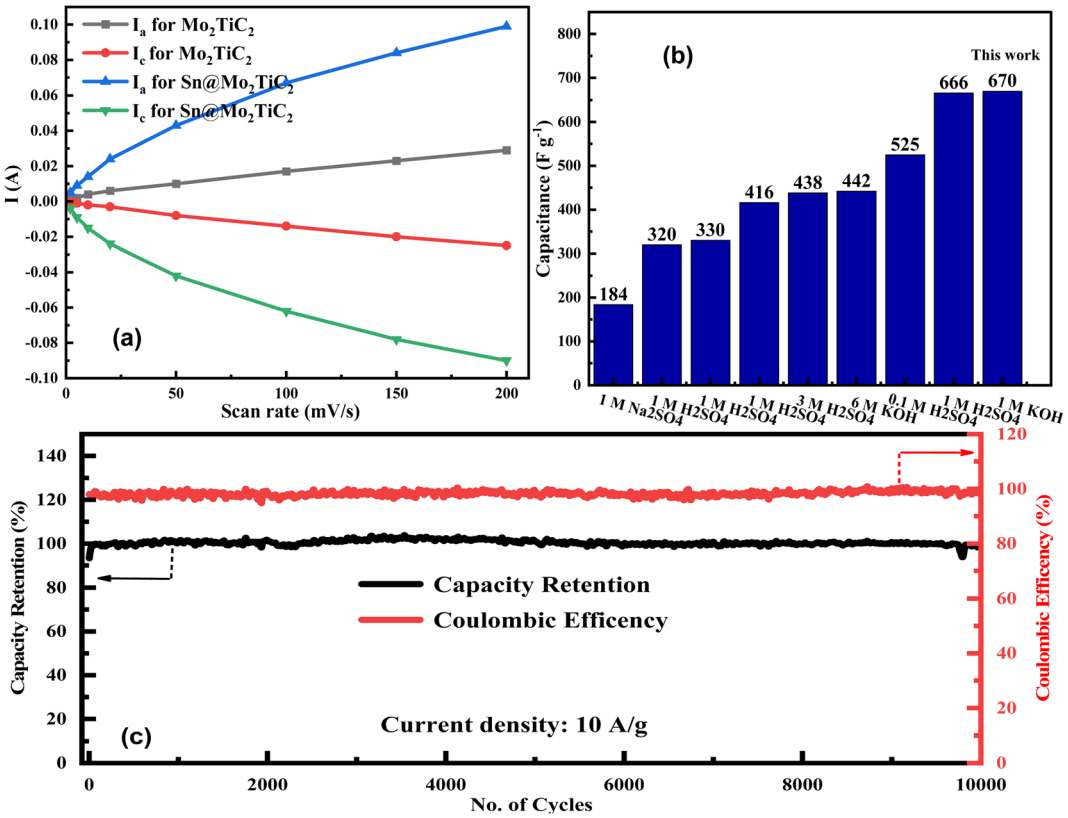

Fig. 6 (a) Anodic and cathodic peak currents *vs.* the scan rates calculated for both Mo_2TiC_2 and $Sn@Mo_2TiC_2$ electrodes. (b) Comparison of our hybrid $Sn@Mo_2TiC_2$ electrode capacitance with the reported data in the literature. (c) Long-term cyclic performance of the $Sn@Mo_2TiC_2$ nanohybrid at current density of 10 A g^{-1}.

compared to Mo_2TiC_2 MXene, which suggests that the charge-storage ability or insertion and extraction of ions were higher in the hybrid electrode due to its good electrochemical activity. The uniform growth of Sn^{2+} on the surface of Mo_2TiC_2 proved helpful to produce more active sites and enhance the contact area with the electrolyte solution to improve the electrochemical performance and kinetics of the redox reaction. Fig. 6b presents a comparison of the already reported data with our hybrid electrode, where the *x*-axis presents the values of different electrolyte solutions used for the various electrochemical studies along with their molar concentrations and the *y*-axis represents the specific capacitance in F g^{-1}. So, our as-synthesized hybrid electrode showed the best charge-storage capacity of about 670 F g^{-1}.[70,73–79] The further extended details of the comparison data are listed in Table 1 in the ESI† which includes the details of the materials and electrolytes used for electrochemical testing along with their achieved specific capacitance.

Table 1 "*d*" and "*c*" values calculated for the 002 plane

Sample	Plane *hkl*	Angle (2θ)	*d* value (nm)	*c*-LP (Å)
Mo_2TiAlC_2	002	9.4	0.94	18.8
Mo_2TiC_2	002	6.8	1.29	25.8
$Sn@Mo_2TiC_2$	002	6.0	1.47	29.3

Fig. 6c shows the long-term cyclic performance of our hybrid electrode $Sn@Mo_2TiC_2$ for 10 000 cycles at a current density of 10 A g^{-1} (with a maximum capacitance of 184 F g^{-1}). The value of capacity retention was observed to remain stable at up to 99% throughout the 10 000 cycles. The intercalated hybrid electrode was observed to be stable electrochemically, which was due to the fast electrolyte transport (through the excessive conductive channels produced due to Sn intercalation) within the electrode, which enhanced its overall capacity retention with no change in the coulombic efficiency of 100%. The values of specific capacitance for our hybrid electrode remained high at all scan rates compared to pristine Mo_2TiC_2 MXene, which demonstrated the enhanced charge-storage capacity of our hybrid material as compared to pure MXene.

The electrochemical conductivity of both samples was examined in 1 M KOH through EIS analysis, as shown in Fig. 7a. The Nyquist plot EIS data were fitted with the Randle plus Warburg series model, and the results in the high-frequency range are also shown in Fig. 7a. Herein, the equivalent circuit, shown in the inset of Fig. 7b, consisted of the charge-transfer resistance R_{ct}, solution resistance R_s, Warburg impedance Z_w related to the diffusion of K^+ ions, and CPE (phase constant element). Both the solution resistance R_s and Warburg impedance Z_w, related to the electrolyte solution and diffusion of electroactive ions, were the same for all the electrodes, but the

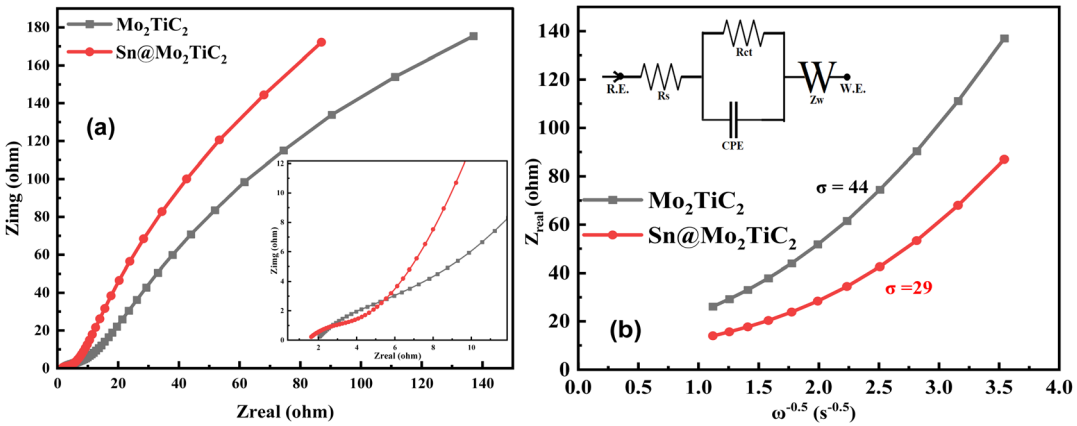

Fig. 7 (a) Nyquist plot of the EIS spectra and inset of the high-frequency region for both Mo_2TiC_2 and $Sn@Mo_2TiC_2$. (b) Real impedance Z_{real} *vs.* $\omega^{-0.5}$ data and in the set equivalent circuit provided for fitting the EIS data for both Mo_2TiC_2 and $Sn@Mo_2TiC_2$.

charge-transfer resistance R_{ct} and CPE were directly influenced by the properties of the hybrid electrode, because they depended on the conductive properties of the as-prepared electrodes.[73] The values of charge-transfer resistance R_{ct} measured for Mo_2TiC_2 and $Sn@Mo_2TiC_2$ were 575 and 292 Ω, respectively. The large difference in the charge-transfer resistance (283 Ω) was basically evidence of the enhanced diffusion process and fast reaction kinetics due to the high electronic conductivity of our as-synthesized hybrid electrode $Sn@Mo_2TiC_2$. Similarly, the value observed for CPE for both the samples Mo_2TiC_2 and $Sn@Mo_2TiC_2$ also increased from 0.0168 to 0.0246 F, respectively.

Fig. 7b shows the plot between the real impedance and frequency $\omega^{-0.5}$, with the plot basically drawn to measure the value of the diffusion coefficient. For that purpose, eqn (SI6) in the ESI† shows the relationship between the real impedance Z_{real} and angular frequency (ω) in the low-frequency regions.[80–82] Here, σ belongs to the Warburg factor, which could be calculated directly from the slope of Fig. 7b. The coefficient of diffusion for K^+ ions was calculated through eqn (SI7) in the ESI† which clarifies the diffusion coefficient is directly proportional to R (gas constant) and T (absolute temperature) and inversely proportional to the A (surface area), n (no. of electrons), F (Faraday constant), C (solution concentration), and D (diffusion coefficient). Here in eqn (SI7) in the ESI† all the factors are constant except "σ", so the value of the diffusion coefficient increases as the σ decreases, so the measured values of σ for Mo_2TiC_2 and $Sn@Mo_2TiC_2$ were 44 and 29, respectively. Because the value of σ for $Sn@Mo_2TiC_2$ was low, the diffusion value of $Sn@Mo_2TiC_2$ was high compared to Mo_2TiC_2; hence the results were also consistent with the EIS Nyquist spectra and cyclic voltammetry data.

Conclusion

We successfully synthesized a $Sn@Mo_2TiC_2$ hybrid *via* the facile liquid-phase pre-intercalated cetyltrimethylammonium bromide (CTAB) method for obtaining enhanced electrochemical properties compared to MXene. Our synthesis method proved successful to enhance the gallery height of Mo_2TiC_2 by increasing the *c*-LP in the case of the hybrid (*c*-LC increased from 25.8 to 29.3 Å) and no additional peak was observed due to Sn^{2+} intercalation, which confirmed the amorphous nanocomplex structure. The TGA results confirmed that our hybrid material was stable up to 500 °C and had a reduced band gap, identifying the interaction between Mo_2TiC_2 and Sn^{2+}, which was studied through UV-vis spectroscopy. The effective surface area of our synthesized nanostructure was also increased from 12 to 30 $m^2\ g^{-1}$ compared to Mo_2TiC_2 MXene. The EDX spectra confirmed the composition of Sn^{2+} in Mo_2TiC_2 and the FTIR spectra also confirmed the presence of Sn^{2+} on Mo_2TiC_2 due to the split in the peak at 750 cm^{-1}. The CV results exhibited the improved electrochemical properties of our hybrid electrode, which was tested for supercapacitor applications. The value of the specific capacitance increased from 212 to 670 F g^{-1} in the case of Mo_2TiC_2 to the $Sn@Mo_2TiC_2$ hybrid and the measured b value also showed the diffusion control mechanism was dominant in the as-prepared hybrid electrode. The cyclic performance of $Sn@Mo_2TiC_2$ was also measured at a current density of 10 A g^{-1}, which was also observed to be stable at up to 99% throughout the 10 000 cycles. The EIS data also showed the low charge-transfer resistance and high diffusion coefficient of the prepared hybrid electrode. The use of MXenes as highly porous and stable electrodes opens the way to construct efficient electronic energy-storage devices.

Author contributions

Irfan Ali managed the whole experimentation and paper writing process; Zulqarnain Haider helped in EIS data collection; Syed Rizwan Hussain supervised the whole project, helped in paper writing, and conceived the research idea.

Conflicts of interest

The authors declared there is no competing interest.

Acknowledgements

The authors thank the Higher Education Commission (HEC) of Pakistan for providing research funding under Project No. 20-14784/NRPU/R&D/HEC/2021.

References

1 L. Grigorios Kyriakopoulos and G. Arabatzis, Electrical Energy Storage Systems in Electricity Generation: Energy Policies, Innovative Technologies, and Regulatory Regimes, *Renewable Sustainable Energy Rev.*, 2016, **56**(C), 1044–1067.

2 Y. Zhang, K. Hu, J. Ren, *et al.*, A Sandwich-Like Si/SiC/Nanographite Sheet as a High-Performance Anode for Lithium-Ion Batteries, *Dalton Trans.*, 2019, **48**, 17683–17690.

3 L. Wu, J. Zheng, L. Wang, *et al.*, PPy-Encapsulated SnS_2 Nanosheets Stabilized by Defects on a TiO_2 Support as a Durable Anode Material for Lithium-Ion Batteries, *Angew. Chem., Int. Ed.*, 2019, **58**, 811.

4 Y. Yu, L. Gu, C. Zhu, S. Tsukimoto, P. A. van Aken and J. Maier, Reversible Storage of Lithium in Silver-Coated Three-Dimensional Macroporous Silicon, *Adv. Mater.*, 2010, **22**, 2247–2250.

5 J. Zhuang, X. Xu, G. Peleckis, W. Hao, S. X. Dou and Y. Du, Silicene: a Promising Anode for Lithium-Ion Batteries, *Adv. Mater.*, 2017, **29**, 1606716.

6 Y. Zhang, Y. Jiang, Y. Li, B. Li, Z. Li and C. Niu, Preparation of Nanographite Sheets Supported Si Nanoparticles by *In Situ* Reduction of Fumed $SiO_2$with Magnesium for Lithium-Ion Battery, *J. Power Sources*, 2015, **281**, 425.

7 Y. Huang, C. Zhu, S. Zhang, *et al.*, Ultrathin Bismuth Nanosheets for Stable Na-Ion Batteries: Clarification of Structure and Phase Transition by *In Situ* Observation, *Nano Lett.*, 2019, **19**, 1118.

8 M. Armand and J. M. Tarascon, Building Better Batteries, *Nature*, 2008, **451**, 652–657.

9 M. S. Whittingham, Lithium Batteries and Cathode Materials, *Chem. Rev.*, 2004, **104**, 4271.

10 J. Luo, C. Wang, H. Wang, X. Hu, E. Matios, X. Lu, W. Zhang, X. Tao and W. Li, Pillared MXene with Ultralarge Interlayer Spacing as a Stable Matrix for High Performance Sodium Metal Anodes, *Adv. Funct. Mater.*, 2019, **29**, 1805946–1805958.

11 A. Geim and K. Novoselov, The Rise of Graphene, *Nat. Mater.*, 2007, **6**, 183–191.

12 B. Radisavljevic, A. Radenovic, J. Brivio, V. Giacometti and A. Kis, Single-Layer MoS_2 Transistors, *Nat. Nanotechnol.*, 2011, **6**, 147–150.

13 K. S. Novoselov, D. Jiang, F. Schedin, T. J. Booth, V. V. Khotkevich, S. V. Morozov and A. K. Geim, Two-Dimensional Atomic Crystals, *Proc. Natl. Acad. Sci. U. S. A.*, 2005, **102**, 10451–10453.

14 R. Ma and T. Sasaki, Nanosheets of oxides and Hydroxides: Ultimate 2D Charge-Bearing Functional Crystallites, *Adv. Mater.*, 2010, **22**, 5082–5104.

15 J. N. Coleman, M. Lotya, A. Neill, S. D. Bergin, P. J. King, U. Khan, K. Young and A. Gaucher, *et.al.*, Two-Dimensional Nanosheets Produced by Liquid Exfoliation of Layered Materials, *Science*, 2011, **331**, 568–571.

16 J. B. Wu, R. Q. Guo, X. H. Huang and Y. Lin, Construction of Self-Supported Porous TiO_2/NiO Core/Shell Nanorod Arrays for Electrochemical Capacitor Application, *J. Power Sources*, 2013, **243**, 317–322.

17 Q. Guo, N. Chen and L. Qu, Two-Dimensional Materials of Group-IVA Boosting the Development of Energy Storage and Conversion, *Carbon Energy*, 2020, **2**, 54–71.

18 J. Ren, Y. Huang and H. Zhu, *et.al.*, Recent Progress on MOF-Derived Carbon Materials for Energy Storage, *Carbon Energy*, 2020, **2**, 176–202.

19 M. Naguib, M. Kurtoglu, V. Presser, J. Lu, J. J. Niu, M. Heon, L. Hultman, Y. Gogotsi and M. W. Barsoum, Two-Dimensional Nanocrystals Produced by Exfoliation of Ti_3AlC_2, *Adv. Mater.*, 2011, **23**, 4248–4253.

20 M. Naguib, O. Mashtalir, J. Carle, V. Presser, J. Lu, L. Hultman, Y. Gogotsi and M. Barsoum, Two-Dimensional Transition Metal Carbides, *ACS Nano*, 2012, **6**, 1322–1331.

21 M. R. Lukatskaya, O. Mashtalir, C. E. Ren, Y. Agnese, P. Rozier, P. L. Taberna, M. Naguib, P. Simon, M. W. Barsoum and Y. Gogotsi, Cation Intercalation and High Volumetric Capacitance of Two-Dimensional Titanium carbide, *Science*, 2013, **341**, 1502–1505.

22 M. Naguib, J. Halim, J. Lu, K. M. Cook, L. Hultman, Y. Gogotsi and M. W. Barsoum, New Two-Dimensional Niobium and Vanadium Carbides as Promising Materials for Li-Ion Batteries, *J. Am. Chem. Soc.*, 2013, **135**, 15966–15969.

23 M. Ghidiu, M. R. Lukatskaya, M. Q. Zhao, Y. Gogotsi and M. W. Barsoum, Conductive Two-Dimensional Titanium Carbide 'Clay' with High Volumetric Capacitance, *Nature*, 2014, **516**, 78–81.

24 Z. Ling, C. E. Ren, M. Q. Zhao, J. Yang, J. M. Giammarco, J. S. Qiu, M. W. Barsoum and Y. Gogotsi, Flexible and Conductive MXene Films and Nanocomposites with High Capacitance, *Proc. Natl. Acad. Sci. U.S.A.*, 2014, **111**, 16676–16681.

25 O. Mashtalir, M. R. Lukatskaya, M. Q. Zhao, M. W. Barsoum and Y. Gogotsi, Amine-Assisted Delamination of Nb_2C MXene for Li-Ion Energy Storage Devices, *Adv. Mater.*, 2015, **27**, 3501–3506.

26 M. Q. Zhao, C. E. Ren, Z. Ling, M. R. Lukatskaya, C. F. Zhang, K. L. Van Aken, M. W. Barsoum and Y. Gogotsi, Flexible MXene/Carbon Nanotube Composite Paper with High Volumetric Capacitance, *Adv. Mater.*, 2015, **27**, 339–345.

27 Q. Tang, Z. Zhou and P. W. Shen, Are MXenes Promising Anode Materials for Li Ion Batteries? Computational Studies on Electronic Properties and Li Storage Capability of Ti_3C_2 and $Ti_3C_2X_2$ (X = F, OH) Monolayer, *J. Am. Chem. Soc.*, 2012, **134**, 16909–16916.

28 X. Zhu, Z. Cao, W. Wang, H. Li, J. Dong, S. Gao, D. Xu, L. Li, J. Shen and M. Ye, Superior-Performance Aqueous Zinc-Ion Batteries Based on the *In Situ* Growth of MnO_2 Nanosheets on V_2CT_X MXene, *ACS Nano*, 2021, **15**, 2971–2983.

29 M. S. Zhu, Y. Huang, Q. H. Deng, J. Zhou, Z. X. Pei, Q. Xue, Y. Huang, Z. F. Wang, H. F. Li, Q. Huang and C. Y. Zhi,

Highly Flexible, Freestanding Supercapacitor Electrode with Enhanced Performance Obtained by Hybridizing Polypyrrole Chains with MXene, *Adv. Energy Mater.*, 2016, **6**, 1600969.

30 X. Liang, A. Garsuch and L. F. Nazar, Surface Cathodes Based on Conductive MXene Nanosheets for High-Performance Lithium–Sulfur Batteries, *Angew. Chem., Int. Ed.*, 2015, **54**, 3907.

31 D. Sun, M. Wang, Z. Li, G. Fan, L.-Z. Fan and A. Zhou, Two-Dimensional Ti_3C_2 as Anode Material for Li-Ion Batteries, *Electrochem. Commun.*, 2014, **47**, 80–83.

32 Y. F. Dong, Z. S. Wu, S. H. Zheng, X. H. Wang, J. Q. Qin, S. Wang, X. Y. Shi and X. H. Bao, Ti_3C_2 MXene-Derived Sodium/Potassium Titanate Nanoribbons for High-Performance Sodium/Potassium ion Batteries with Enhanced Capacities, *ACS Nano*, 2017, **11**(5), 4792–4800.

33 J. Wang, J. Tang, B. Ding, V. Malgras, Z. Chang, X. D. Hao, Y. Wang, H. Dou, X. G. Zhang and Y. Yamauchi, Hierarchical Porous Carbons with Layer-By-Layer Motif Architectures from Confined Soft-Template Self-Assembly in Layered Materials, *Nat. Commun.*, 2017, **8**, 15717.

34 C. F. Zhang, B. Anasori, A. Seral-Ascaso, S. H. Park, N. McEvoy, A. Shmeliov, G. S. Duesberg, J. N. Coleman, Y. Gogotsi and V. Nicolosi, Transparent, Flexible, and Conductive 2D Titanium Carbide (MXene) Films with High Volumetric Capacitance, *Adv. Mater.*, 2017, **29**, 1702678.

35 X. H. Wu, Z. Y. Wang, M. Z. Yu, L. Y. Xiu and J. S. Qiu, Stabilizing the MXenes by Carbon Nanoplating for Developing Hierarchical Nanohybrids with Efficient Lithium Storage and Hydrogen Evolution Capability, *Adv. Mater.*, 2017, **29**, 1607017.

36 R. T. Wang, S. J. Wang, Y. B. Zhang, D. D. Jin, X. Y. Tao and L. Zhang, Graphene Coupled Ti_3C_2 MXenes-Derived TiO_2 Mesostructure: Promising Sodium-Ion Capacitor Anode with Fast Ion Storage and Long-Term Cycling, *J. Mater. Chem. A*, 2018, **6**, 1017.

37 J. Luo, X. Tao, J. Zhang, Y. Xia, H. Huang, L. Zhang, Y. Gan, C. Liang and W. Zhang, Sn4+ ion Decorated Highly Conductive Ti_3C_2 MXene: Promising Lithium-Ion Anodes with Enhanced Volumetric Capacity and Cyclic Performance, *ACS Nano*, 2016, **10**, 2491–2499.

38 J. Luo, C. Fang, C. Jin, H. Yuan, O. Sheng, R. Fang, W. Zhang, H. Huang, Y. Gan, Y. Xia, C. Liang, J. Zhang, W. Li and X. Tao, Tunable Pseudocapacitance Storage of MXene by Cation Pillaring for High Performance Sodium-Ion Capacitors, *J. Mater. Chem. A*, 2018, **6**, 7794.

39 B. Li, D. Zhang, Y. Liu, Y. Yu, S. Li and S. Yang, Flexible Ti_3C_2 MXene-Lithium Film with Lamellar Structure for Ultrastable Metallic Lithium Anodes, *Nano Energy*, 2017, **39**, 654–661.

40 H. Liu, C. Y. Duan, C. H. Yang, W. Q. Shen, F. Wang and Z. F. Zhu, A Novel Nitrite Biosensor Based on the Direct Electrochemistry of Hemoglobin Immobilized on MXene-Ti_3C_2, *Sens. Actuators, B*, 2015, **218**, 60–66.

41 F. Wang, C. H. Yang, C. Y. Duan, D. Xiao, Y. Tang and J. F. Zhu, An Organ-Like Titanium Carbide Material (MXene) with Multilayer Structure Encapsulating Hemoglobin for a Mediator-Free Biosensor, *J. Electrochem. Soc.*, 2015, **162**, B16–B21.

42 F. Shahzad, M. Alhabeb, C. B. Hatter, B. Anasori, S. M. Hong, C. M. Koo and Y. Gogotsi, Electromagnetic Interference Shielding with 2D Transition Metal Carbides (MXenes), *Science*, 2016, **353**, 1137–1140.

43 J. Liu, H. B. Zhang, R. H. Sun, Y. F. Liu, Z. S. Liu, A. G. Zhou and Z. Z. Yu, Hydrophobic, Flexible, and Lightweight MXene Foams for High-Performance Electromagnetic Interference Shielding, *Adv. Mater.*, 2017, **29**, 1702367.

44 Q. R. Zhang, J. Teng, G. D. Zou, Q. M. Peng, Q. Du, T. F. Jiao and J. Y. Xiang, Efficient Phosphate Sequestration for Water Purification by Unique Sandwich-like MXene/Magnetic Iron Oxide Nanocomposites, *Nanoscale*, 2016, **8**, 7085–7093.

45 C. E. Ren, K. B. Hatzell, M. Alhabeb, Z. Ling, K. A. Mahmoud and Y. Gogotsi, Charge and Size-Selective Ion Sieving Through $Ti_3C_2T_x$ MXene Membranes, *J. Phys. Chem. Lett.*, 2015, **6**, 4026–4031.

46 K. Rasool, M. Helal, A. Ali, C. E. Ren, Y. Gogotsi and K. A. Mahmoud, Antibacterial Activity of $Ti_3C_2T_x$ MXene, *ACS Nano*, 2016, **10**, 3674–3684.

47 M. Naguib, M. Kurtoglu, V. Presser, J. Lu, J. Niu, M. Heon, L. Hultman, Y. Gogotsi and M. W. Barsoum, Two-Dimensional Nanocrystals Produced by Exfoliation of Ti_3AlC_2, *Adv. Mater.*, 2011, **23**, 4248–4253.

48 M. Naguib and Y. Gogotsi, Synthesis of Two-Dimensional Materials by Selective Extraction, *Acc. Chem. Res.*, 2015, **48**, 128–135.

49 Q. Peng, J. Guo, Q. Zhang, J. Xiang, B. Liu, A. Zhou, R. Liu and Y. Tian, Unique Lead Adsorption Behavior of Activated Hydroxyl Group in Two-Dimensional Titanium Carbide, *J. Am. Chem. Soc.*, 2014, **136**, 4113–4116.

50 J. T. Kloprogge, Synthesis of Smectites and Porous Pillared Clay Catalysts, A Review, *J. Porous Mater.*, 1998, **5**, 5–41.

51 A. Gil, L. M. Gandia and M. A. Vicente, Recent Advances in the Synthesis and Catalytic Applications of Pillared Clays, *Catal. Rev.*, 2000, **42**, 145–212.

52 J. Cheng, S. Ming Yu and P. Zuo, Horseradish Peroxidase Immobilized on Aluminum-Pillared Interlayered Clay for the Catalytic Oxidation of Phenolic Wastewater, *Water Res.*, 2006, **40**, 283–290.

53 J. Luo, W. Zhang, H. Yuan, C. Jin, L. Zhang, H. Huang, C. Liang, Y. Xia, J. Zhang, Y. Gan and X. Tao, Pillared Structure Design of MXene with Ultra-Large Interlayer Spacing for High Performance Lithium-Ion Capacitors, *ACS Nano*, 2017, **11**(3), 2459–2469.

54 J. Luo, C. Wang, H. Wang, X. Hu, E. Matios, X. Lu, W. Zhang, X. Tao and W. Li, Pillared MXene with Ultralarge Interlayer Spacing as a Stable Matrix for High Performance Sodium Metal Anodes, *Adv. Funct. Mater.*, 2019, **29**, 1805946.

55 P. A. Maughan, L. Bouscarrat, V. R. Seymour, S. Shao, S. J. Haigh, R. Dawson, N. Tapia-Ruiz and N. Bimbo, Pillared Mo_2TiC_2 MXene for high-power and long-life lithium and sodium-ion batteries, *Nanoscale Adv.*, 2021, **3**, 3145–3158.

56 P. A. Maughan, N. T. Ruiz and N. Bimbo, *In situ* Pillared MXene as a Viable Zinc-Ion Hybrid Capacitor, *Electrochim. Acta*, 2020, **341**, 136061.

57 J. Luo, J. Zheng, J. Nai, C. Jin, H. Yuan, O. Sheng, Y. Liu, R. Fang, W. Zhang, H. Huang, Y. Gan, Y. Xia, C. Liang, J. Zhang, W. Li and X. Tao, Atomic Sulfur Covalently Engineered Interlayers of Ti_3C_2 MXene for Ultra-Fast Sodium-Ion Storage by Enhanced Pseudocapacitance, *Adv. Funct. Mater.*, 2019, **29**, 1808107.

58 B. Anasori, M. R. Lukatskaya and Y. Gogotsi, 2D Metal Carbides and Nitrides (MXenes) for Energy Storage, *Nat. Rev. Mater.*, 2017, **2**, 16098.

59 H. Kim, B. Anasori, Y. Gogotsi and H. N. Alshareef, Thermoelectric Properties of Two-Dimensional Molybdenum-Based MXenes, *Chem. Mater.*, 2017, **29**, 6472–6479.

60 M. Naguib, R. R. Unocic, B. L. Armstrong and J. Nanda, Large-Scale Delamination of Multi-Layers Transition Metal Carbides and Carbonitrides MXenes, *Dalton Trans.*, 2015, **44**, 9353–9358.

61 X. H. Wang and Y. C. Zhou, Stability, and Selective Oxidation of Aluminum in Nano Laminate Ti_3AlC_2 Upon Heating in Argon, *Chem. Mater.*, 2003, **15**, 3716–3720.

62 J. Yu Si, B. Tawiah, W. L. Sun, B. Lin, C. Wang, A. C. Y. Yuen, B. Y. A. Li, W. Yang and H. D. Lu, *et.al.*, Functionalization of MXene Nanosheets for Polystyrene Towards High Thermal Stability and Flame Retardant Properties, *J. Polym.*, 2019, **11**, 976.

63 V. Chaudhary, A. Gautam, Y. K. Mishra and A. Kaushik, Emerging MXene Polymer Hybrid Nanocomposites for High-Performance Ammonia Sensing and Monitoring, *J. Nanomater.*, 2021, **11**, 2496.

64 X. Jiang, A. V. Kuklin, A. Baev, Y. Ge, H. Agren, H. Zhang and P. N. Prasad, Two-Dimensional MXenes: From Morphological to Optical, Electric, and Magnetic Properties and Applications, *Phys. Rep.*, 2020, **848**, 1–58.

65 P. A. Maughan, V. R. Seymour, R. Bernardo, Gavito, D. J. Kelly, S. Shao, S. Tantisriyanurak, R. Dawson, S. J. Haigh, R. J. Young, N. Tapia-Ruiz and N. Bimbo, Porous Silica-Pillared MXenes with Controllable Interlayer Distances for Long-Life Na-Ion Batteries, *Langmuir*, 2020, **36**(16), 4370–4382.

66 Z. U. D. Babar, J. Fatheema, N. Arif, M. S. Anwar, S. Gul, M. Iqbal and S. Rizwan, Magnetic Phase Transition from Paramagnetic in Nb_2AlC-MAX to Superconductivity-Like Diamagnetic in Nb_2C-MXene: An Experimental and Computational Analysis, *RSC Adv.*, 2020, **10**, 25669.

67 H. Kim, B. Anasori, Y. Gogotsi and H. N. Alshareef, Thermoelectric Properties of Two-Dimensional Molybdenum-Based MXenes, *Chem. Mater.*, 2017, **29**, 6472–6479.

68 C. Chen, *et al.*, MoS_2-on-MXene Heterostructures as Highly Reversible Anode Materials for Lithium-Ion Batteries, *Angew. Chem., Int. Ed.*, 2018, **57**, 1846–1850.

69 Q. X. Xia, J. Fu, J. M. Yun, R. S. Maneb and K. H. Kim, High Volumetric Energy Density Annealed-MXene Nickel Oxide/MXene Asymmetric Supercapacitor, *RSC Adv.*, 2017, **7**, 11000–11011.

70 A. Zaheer, S. A. Zahra, M. Z. Iqbal, A. Mahmood, S. A. Khan and S. Rizwan, Nickel-Adsorbed Two-Dimensional Nb2C MXene for Enhanced Energy Storage Applications, *RSC Adv.*, 2022, **12**, 4624.

71 S. A. Zahra, B. Anasori, M. Z. Iqbal, F. Ravaux, A. Tarawneh and M. S. Rizwana, Enhanced Electrochemical Performance of Vanadium Carbide MXene Composites for Supercapacitors, *APL Mater.*, 2022, **10**, 060901.

72 R. Li, X. Yu, X. Bian and F. Hu, Preparation, and Electrochemical Performance of VO_2 Hollow Spheres as a Cathode for Aqueous Zinc Ion Batteries, *RSC Adv.*, 2019, **9**, 35117.

73 T. Yaqoob, M. Rani, A. Mahmood, R. Shafique, S. Khan, N. K. Janjua, A. A. Shah, A. Ahmad and A. A. Al-Kahtani, MXene/Ag_2CrO_4 Nanocomposite as Supercapacitors Electrode, *Materials*, 2021, **14**, 6008.

74 X. Zang, J. Wang, Y. Qin, T. Wang, C. He, Q. Shao, H. Zhu and N. Cao, Enhancing Capacitance Performance of $Ti_3C_2T_x$ MXene as Electrode Materials of Supercapacitor: From Controlled Preparation to Composite Structure Construction, *Nano-Micro Lett.*, 2020, **12**, 77.

75 Y. Dall'Agnese, M. R. Lukatskaya, K. M. Cook, P. L. Taberna, Y. Gogotsi and P. Simon, High Capacitance of Surface Modified 2D Titanium Carbide in Acidic Electrolyte, *Electrochem. Commun.*, 2014, **48**, 118–122.

76 C. Zhang, *et al.*, Synthesis and Charge Storage Properties of Hierarchical Niobium Pentoxide/Carbon/Niobium Carbide (MXene) Hybrid Materials, *Chem. Mater.*, 2016, **28**(11), 3937–3943.

77 M. Boota, B. Anasori, C. Voigt, M. Q. Zhao, M. W. Barsoum and Y. Gogotsi, Pseudocapacitive Electrodes Produced by Oxidant-Free Polymerization of Pyrrole Between the Layers of 2D Titanium Carbide (MXene), *Adv. Mater.*, 2016, **28**, 1517–1522.

78 X. Wang, Q. Fu, J. Wen, X. Ma, C. Zhu, X. Zhang and D. Qi, 3D Ti_3C_2Txaerogels with Enhanced Surface Area For High Performance Supercapacitors, *Nanoscale*, 2018, **10**, 20828–20835.

79 M. Fatima, *et al.*, Nb-Doped MXene with Enhanced Energy Storage Capacity and Stability, *Front. Chem.*, 2020, **8**, 1–8.

80 H. Liu, *et al.*, Kinetic Study on $LiFePO_4$/C Nanocomposites Synthesized by Solid State Technique, *J. Power Sources*, 2006, **159**, 717–720.

81 A. J. Bard and L. R. Faulkner, *Electrochemical Methods*, John Wiley & Sons, Inc., 2001, 2 edn, p. 211.

82 S. Khamsanga1, R. Pornprasertsuk, T. Yonezawa, A. A. Mohamad and S. Kheawhom, δ-MnO_2 nanofower/Graphite Cathode for Rechargeable Aqueous Zinc Ion Batteries, *Sci. Rep.*, 2019, **9**, 8441.